Journal of Engineering Science and Technology
Vol. 9, No. 1 (2014) 47 - 63

FINITE ELEMENT ANALYSIS ON THE EFFECT OF SOLDER JOINT GEOMETRY FOR THE RELIABILITY OF BALL GRID ARRAY ASSEMBLY WITH FLEXIBLE AND RIGID PCBS

CHUN-SEAN LAU*, M. Z. ABDULLAH, M. ABDUL MUJEEBU, N. MD. YUSOP

School of Mechanical Engineering, Universiti Sains Malaysia, Engineering Campus, 14300 Nibong Tebal, Penang, Malaysia
*Corresponding Author: chun_sean@hotmail.com

Abstract

In the present study, three-dimensional (3D) finite element simulation on 132 PIN fleXBGATM package was performed to predict the effect of solder joint geometry on the reliability of Ball Grid Array (BGA) solder joints on flexible and rigid PCBs subjected to thermo-cyclic loading. The commercial FEA tool ABAQUS Version 6.9 was used for the simulations of various shapes of solder joints such as barrel, column and hourglass. Apart from a global modeling, the submodeling analysis technique (local modeling) was also used on the critically affected solder joints, in order to enhance the computation efficiency. The accumulated creep strain and strain energy density were observed for each case, and optimum geometries were obtained. The model was validated with the published experimental data with the minimum percentage error of 3%. It was observed that the hourglass solder joint geometry was very crucial on the reliability of BGA solder joints, and for a given PCB, the optimal choice of hourglass solder joint geometry depended on its rigidity.

Keywords: Finite element simulation, Ball grid array (BGA), Solder joint geometry, Flexible PCB, Submodeling analysis technique.

1. Introduction

Tin-based eutectic and lead-free solder joints are used in the ball grid array (BGA) packages to ensure electrical and mechanical functionalities between the packages and the PCB [1-2]. Alternating strains and stresses caused by mismatch of coefficient of thermal expansion are the main causes of failure in solder joint interconnections. Several factors have been found to be affecting the solder joint reliability, such as solder joint geometry, board material, chip size, interface metallurgy, and underfill

Nomenclatures

A	Power Law multiplier, s^{-1}
B	Hyperbolic law multiplier, MPa^{-1}
D	Pad diameter, mm
H	Standoff height of the solder joint, mm
M	Midpoint diameter of solder joint, mm
n	Stress order
R	Universal gas constant, J/mol.K
V_T	Volume of barrel-shaped solder joint, mm^3
U_x, U_y, U_z	Velocity component in x, y, z directions, mm/s

Greek Symbols

ΔH	Activation energy, J/mol
ΔW	Accumulated strain energy density per cycle of each element, MPa
ΔW_{ave}	Average accumulated strain energy density per cycle for the interface elements, PSI
ΔW_{max}	Accumulated strain energy density per cycle of critical element, MPa
$\dot{\varepsilon}_{eq}$	Equivalent strains
Θ	Temperature of thermal load, K
Θ^z	User-defined value of absolute zero on the temperature scale used, K
σ_{eq}	Equivalent stresses, MPa
σ_w	Fatigue life, cycles
Φ_c	Diameter of copper pad, mm
Φ_s	Diameter of midpoint solder joint, mm

and substrate materials [3]. However, very little work is found in the open literature, on the solder joint reliability analysis of flexible electronics [4]. The flexible printed circuit board (FPCB) has unique capabilities including reduced board thickness, added "twist" of flexibility and vibration resistance. This lightness, and ability to bend to various shapes, make FPCB play vital role in electronic product miniaturization and replace rigid boards (RPCB) in numerous electronic devices [4].

Liu and Lu [5] found that solder joint geometry characterized by shape and standoff height is the dominant factor affecting solder joint reliability. Several approaches, such as stacked solder, double bump technology, stretched solder, ceramic column grid array and second-reflow-process approach [6] were reported to increase the standoff height and control the shape of solder bump connection. The stacked solder technique used the bump-limiting metal pads to separate solder bump at different level by sequential stacking process [7]. Double bump technology entailed the controlled overlapping of two molten solder bumps on both surfaces to form nearly cylindrical joint [8]. A mechanical standoff was used in this technique to control the final separation between packages and PCB. A cost effective stretch solder joint involved the process of stretching the solder joint to acquire hourglass shape and greater standoff height [9]. Liu and Lu [5]

demonstrated that hourglass shape solders had the lowest plastic strain and better reliability during thermal cycling. For the constant solder volume and pad size, hourglass-shaped solder joint had the greatest standoff height, followed by column and barrel shaped solder joint.

Accelerated thermal cycling (ATC) tests have been widely used in the electronics industry to assess the reliability of new electronic products against the low-cycle fatigue in field environment [10]. However, this test method is expensive and time consuming. With the maturity of numerical techniques, the failure of solder joints could easily be predicted by simulations without resorting to lengthy and costly tests. Over the past decades, the validity of finite element analysis (FEA) has been discussed by many researchers [11-13]. Ridout and Bailey [10] reviewed various modeling methods to predict solder joint failure, such as analytical method, constitutive law plus fatigue law methods, and damage mechanics based methods [14]. The analytical method proposed by Engelmaier [15] for predicting the lifetime of 63Sn37Pb joints was recommended in the IPC-D-279 standard. The damage mechanics based methods allowed crack paths to be predicted. A review of covering several methods has provided by Desai and Whitenack [16].

Constitutive law plus fatigue law methods work by running transient simulation with FEM tools such as MSC/NASTRAN, ANSYS or ABAQUS to predict the solder's stress strain behavior during a thermal cycle. The standard method for FEA of solder joints involves only the modeling of steady-state creep, which could provide a reasonable prediction. Many authors [17] have used hyperbolic sine creep to capture the change in creep mechanism. Darveaux et al. [18] have published constants for four different alloys including SnPb and Sn3.5Ag. From this prediction, either the accumulated effective plastic strain per cycle or the accumulated strain energy density per cycle of each element (ΔW) was extracted to be used in a fatigue law. Lee et al. [19] reviewed various fatigue laws; the simplest fatigue laws were the Coffin–Manson law and the strain energy based law, used by Akay et al. [11]. Darveaux [20] fatigue law predicted the time taken for crack initiation, and crack propagation rate by averaging ΔW over a layer of solder 25 μm thick adjacent to the package interface where the cracks were expected to develop.

As far as the authors are aware, the effect of solder joint geometry on the reliability of BGA solder joints on FPCB has less reported so far [21-23]. Accordingly, in the present study, three-dimensional (3D) finite element simulation on 132-PIN fleXBGATM package is performed considering both FPCB and RPCB [24-25]. The commercial FEA tool ABAQUS Version 6.9 is used for the simulations of various shapes of solder joints such as barrel, column and hourglass. Furthermore, the submodeling analysis technique [26] is used to enhance the computation efficiency. The accumulated creep strain and strain energy density are observed for each case, and optimum geometries are obtained. The model is validated with the published experimental data [24] with acceptable error.

2. Materials and Methods

2.1. Package dimensions

Figure 1 shows the fleXBGATM assembly [24] and Fig. 2 shows the 3D quarter of a fleXBGATM component. It has 132 tin-lead (63Sn37Pb) eutectic solder

joints which are interconnected by 66 couples of shorted copper pads on the BT substrate without underfill. The multi-layer FPCB is made of polyimide and copper materials with a minimum thickness of 0.31mm whereas RPCB is made of 4 layers FR-4 material (2S2P) with a thickness of 1.6 mm. The detailed dimensions of the package are summarized in Table 1.

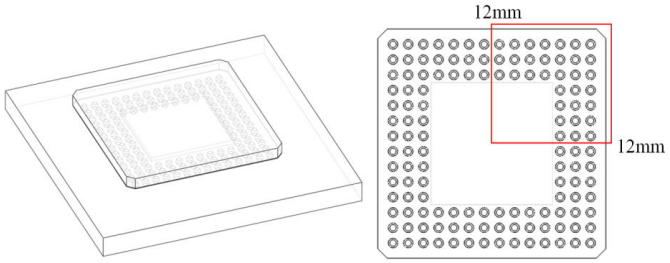

Fig. 1. FleXBGATM Assembly.

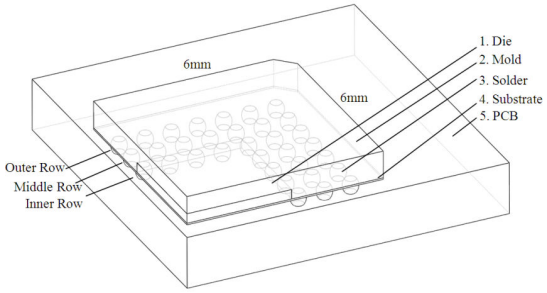

Fig. 2. 3D Quarter of a FleXBGATM Component.

Table 1. Dimensions of the FleXBGATM Package.

Material	Dimensions (mm)
RPCB	1.6×140×120
FPCB	0.31×140×120
Copper pad	Φ_c=0.33
63Sn37Pb solder joint	Height= 0.4 Φ_s=0.4572, Pitch= 0.8
BT substrate	0.05×12×12
Silicon die	0.3×6.4×6.4
Molding compound	0.84×12×12

2.2. Package materials and properties

The molding compound, silicon die, BT substrate and RPCB (FR-4) are assumed as isotropic linear elastic materials whose properties are listed in Table 2 [11, 12, 25]. The equivalent material property of polyimide based multi-layer FPCB was predicted by Pan and Vatanporast [27], as shown in Table 2. The coefficients of thermal expansion (CTE) for various materials are shown in Table 3.

Table 2. Properties of Constituent Materials.

Material		Young's Modulus (MPa)	Poisson's ratio
PCB	FPCB: Polyimide [27]	5225	0.25
	RPCB: FR-4 [25]	18200	0.25
Leaded Solder	63Sn37Pb [1]	23250 (373K) 19000 (423K)	0.36 (373K) 0.36 (423K)
Substrate	BT Substrate [11]	26000	0.39
Die	Silicon [12]	130360	0.28
Mold	Molding Compound [12]	16520	0.25

Table 3. Coefficient of Thermal Expansion (CTE) for Various Solders.

Material	Temperature (K)	CTE (ppm/K)
63Sn37Pb [1]	293	24.0
	423	26.9
FPCB: Polyimide [27]	-	26.1
RPCB: FR-4 [25]	-	15
BT Substrate [11]	-	15
Silicon [12]	-	2.5
Molding Compound [12]	-	14.8

Since the solder temperature is assumed to be above half of its melting point, time-dependent creep processes are expected to dominate the deformation kinetics. A hyperbolic sine creep law [1, 16] is used to study the evolution and accumulation of irreversible strains and energies of solder joints made of various types of solder:

$$\dot{\varepsilon}_{eq} = A(\sinh B\sigma_{eq})^{\mathrm{n}} \exp(-\frac{\Delta H}{R(\theta-\theta^{z})}) \quad (1)$$

where $\dot{\varepsilon}_{eq}$ is equivalent strains, σ_{eq} is equivalent stresses, θ is the temperature, θ^{z}, the user-defined value of absolute zero on the temperature scale used, R is the universal gas constant, A is Power Law multiplier, B is hyperbolic law multiplier, n is the stress order and ΔH is the activation energy. Besides, A, B, n and ΔH represent the characteristics for the secondary creep behavior of a particular solder. The values A, B, n and ΔH and R for the 63Sn37Pb solder used in the present study are listed in Table 4 [1].

Note that this type of creep constitutive equation ignores transient creep effects and assumes steady-state creep after the beginning of loading. This might be deficient in studying creep under thermal stress reversals. Besides, for thermal load cycles with a period of 3600s, the creep dominates and the instantaneous time-independent plasticity is assumed as insignificant; this would suggest that the common practice of ignoring instantaneous plasticity is justified [10].

Table 4. Creep Law Constants of Various Solders [1].

Solder	A (s^{-1})	B (MPa^{-1})	n	ΔH(J/mol)	R (J/mol.K)
63Sn37Pb	96200	0.086956	3.3	67390	8.314

2.3. FEA modelling

The following three steps are carried out in the present ABAQUS modeling:

Step 1: Global modeling: The purpose of global modeling is to identify the critical local ball and to provide driving boundary conditions for the subsequent submodeling analysis. For the symmetrical plane, the global model comprised one-fourth of the entire package as shown in Figure 3(a). Meshing is done with C3D8R Hexahedral element with 23,991 elements, which contributed by 30,227 nodes. Symmetrical boundary conditions are applied along the centre line of the PCB, and node of diagonal bottom corner of PCB is constrained with boundary condition $U_x = U_y = Uz = 0$ to prevent free body translation.

Step 2: Local modeling: The local model contains the most critical solder joint located in the package, where the maximum accumulated creep strains (CEEQ) take place. The width of the local model is equal to the solder joint pitch. Figure 3(b) shows the higher mesh density of local model (1,588 nodes and 1,233 elements).

Step 3: Accumulated strain energy density per cycle of critical element (ΔW_{max}) obtained for various shapes of solder geometry are used to predict optimum geometry of the solder joint.

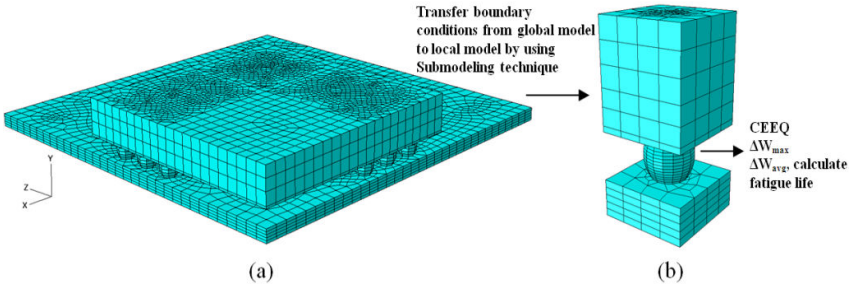

Fig. 3. (a) 3D Global Model (Quarter of the Whole Package), (b) 3D Local Model.

2.4. Various solder joint geometries

The geometry of the solder joints is described by two non-dimensional parameters, the aspect ratio (AR) and the shape factor (SF) [9], which are defined as:

$$\text{Aspect ratio } (AR) = \frac{H}{D} \quad (2)$$

$$\text{Shape Factor } (SF) = \frac{M}{D} \quad (3)$$

where H is the standoff height of the solder joint, D is the pad diameter and M is the midpoint diameter of solder joint. SF essentially describes the profile of the solder joint.

In this work, five solder joint geometries (Table 5) are generated to study their effect on CEEQ. The conventional barrel shape is chosen as the reference with specifications as shown in Fig. 4. Assuming H = 0.4 mm, the volume of barrel-

shaped solder joint (V_T) [28] could be calculated from Eq. (4) by knowing D, M and H

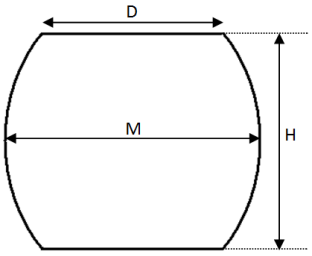

Fig. 4. Barrel Shape Solder Joint with Specifications.

$$V_T = \frac{\pi H}{12}(2M^2 + D^2) \quad (4)$$

then the value of H for the other geometries are estimated by using the truncated ellipsoid model [25] as expressed in Eq. (5).

$$H = \frac{15V_T}{\pi(2M^2+MD+0.75D^2)} \quad (5)$$

Keeping V_T and D fixed, when M is reduced, the barrel shape successively takes different shapes with increasing H, such as, Column, Hourglass 1, Hourglass 2 and Hourglass 3, as shown in Table 5.

Table 5. Various Solder Joint Geometries with Specifications [28].

	Barrel	Column	Hourglass 1	Hourglass 2	Hourglass 3
Solder joint geometry	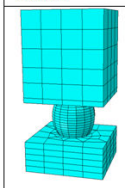	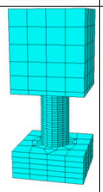	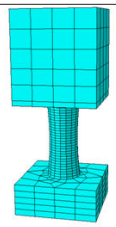	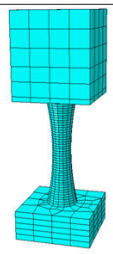	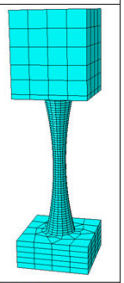
AR	1.212	1.955	2.353	3.519	4.681
SF	1.385	1.000	0.866	0.604	0.436
M (mm)	0.4572	0.3300	0.2858	0.1993	0.1439
H (mm)	0.400	0.645	0.776	1.161	1.545

2.5. Thermo-cyclic loading

The thermal cycling conditions applied in the present study are the same as those used by Darveaux et al. [24]. The temperature profile in Fig. 5 shows a range 233 to 398 K at 1 cycle/hour (1 cph), with 15 min dwell time at the extreme temperatures and 11oC/min ramp rate. The reference temperature for the stress free state is 298 K [25].

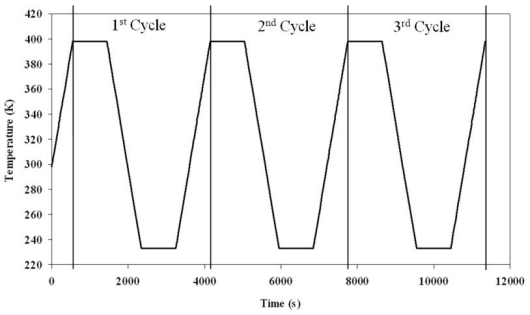

Fig. 5. Temperature Cycle Profile.

3. Results and Discussion

3.1. Grid independence test

Grid independence test is carried out on the global model meshes for FPCB and RPCB. The FPCB and RPCB meshes are declared independent when the maximum CEEQ and maximum displacement did not change by more than ± 0.1% between successive meshes. The summary of grid independence test for FPCB meshes is presented in Table 6. Case 5 being the finest in grid size, the deviations in maximum CEEQ and maximum displacement of cases 1, 2, 3 and 4 from case 5 are checked, and accordingly, case 4 (23,991 meshes) is found to be acceptable, as evident from Table 6. By following similar procedure, the mesh size for RPCB is adopted as 24,151 (case 4 in Table 7).

Table 6. Summary of Grid Independence Test for FPCB Meshes.

Case	1	2	3	4	5
Elements	10,091	13,566	20,516	23,991	27,466
Maximum CEEQ	0.11730	0.09890	0.09750	0.09737	0.09740
Deviation from case 5 (%)	20.431	1.540	0.103	0.030	0.00
Maximum displacement	0.07880	0.04690	0.04750	0.04756	0.04760
Deviation from case 5 (%)	65.546	1.471	0.210	0.084	0.00

Table 7. Summary of Grid Independence Test for RPCB Meshes.

Case	1	2	3	4	5
Elements	10,119	13,626	20,640	24,151	27,654
Maximum CEEQ	0.07916	0.08666	0.08568	0.08558	0.08557
Deviation from case 5 (%)	7.491	1.274	0.129	0.012	0.00
Maximum displacement	0.03260	0.02131	0.02130	0.02128	0.02128
Deviation from case 5 (%)	53.195	0.141	0.094	0.00	0.00

3.2. Verification of submodeling

The submodeling procedure [26] in the current simulation is verified by means of a two dimensional (2D) FEA model, meshed with quadrilateral elements, as shown in Fig. 6; the material properties are same as in Section 2.2.

Due to axis-symmetric geometry, the global model represents only half of the package length. For verification purpose, scales of the FE meshes on the global model and the local model are set identical. The 2D FEA model is subjected to the same cyclic thermal load as mentioned in Section 2.5.

Figure 7 shows hysteresis loops of shear stresses versus creep shear strains for critical element, and Fig. 8 depicts the history of the accumulated volume-weighted average creep energy density for the thin layer of critical solder joint. These two quantities are broadly applied in numerical assessments of fatigue life or reliability study on solder joint. Clearly, results from the global model matched those from the local model precisely, indicating that the preset submodeling procedure is valid.

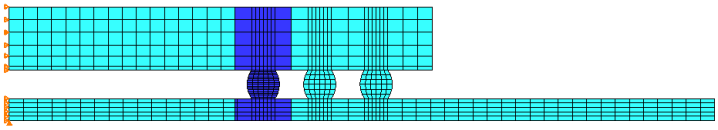

Fig. 6. Finite Element Meshes for the 2D Global and Local Model.

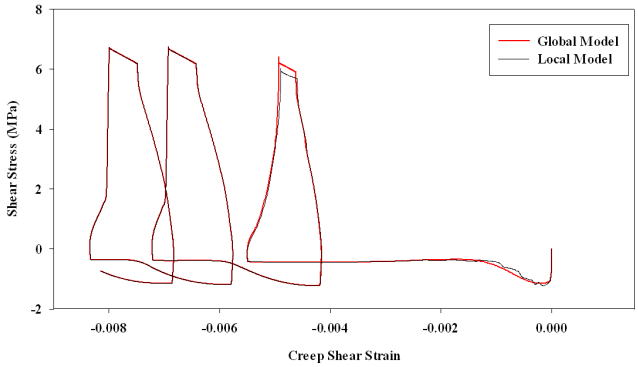

Fig. 7. Hysteresis Loops of Shear Stresses vs. Creep Shear Strains.

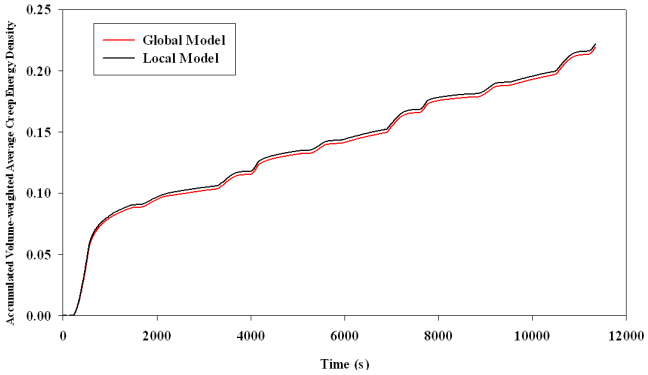

Fig. 8. Accumulated Volume-weighted Average Creep Energy Density vs. Time.

3.3. Comparison with previous experiments

The present simulations are substantiated by previous experimental results. As no reference data is available for FPCB, validation is performed in the case of RPCB for CEEQ pattern and fatigue life. As illustrated in Fig. 9, the failure locations in

solder joints of barrel, column and hourglass shapes match well with the experimental observations [9]. This matching is presumed to testify the validity of simulations on FPCB as well. The fatigue life (σ_w) for barrel shape is also estimated in ABAQUS, by using the Darveaux Fatigue law (applicable only for barrel shape), and the results are compared with the published experimental data [24], as presented in Table 8. It shows that the present predictions are in acceptable agreement with the experimental data, as the variations are within 25% [20]. The discrepancy may be attributed to the factors such as, experimental errors, the use of "equivalent" material properties for the BT substrate, RPCB and FPCB, the material properties assumed in the FE modeling, etc.

Table 8. Comparison of Predicted and Experimental Results of Fatigue Life for Barrel Shape.

Data Set	Fatigue life, σ_w (cycles)		Difference (%)
	Experiment [24]	Present simulation	
11	2998	2908	3.00
17	2967	2277	23.26
29	708	622	12.15

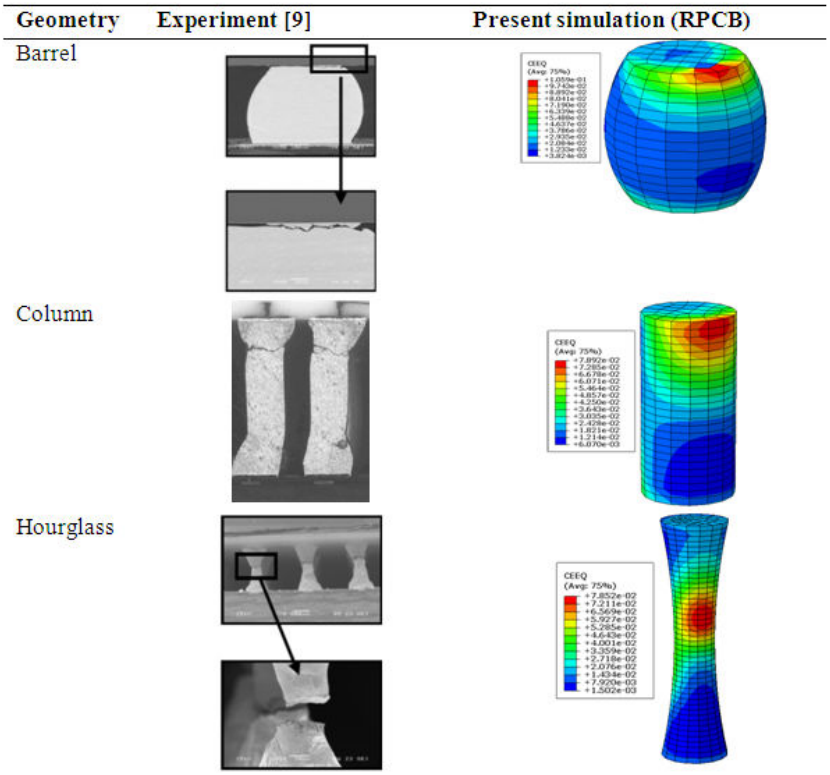

Fig. 9. Comparison of Experimental Crack Locations with the Present Predictions.

3.4. Accumulated creep strain (CEEQ)

The locations of critically affected solder joints (maximum CEEQ) for different solder joint geometries in FPCB and RPCB at the end of the third cycle are shown in Fig. 10, and the corresponding creep strain contours, are shown in Fig. 11. For RPCB, locations of critically affected joints remain constant (at the inner row, as in Fig. 10), whereas for FPCB, it changes according to the geometry. The joints having maximum CEEQ are most likely to fail first [18]. Figure 11 indicates that, the crack locations of solder joints on RPCB shift from the chip-solder interface to the midpoint of the solder joint when the aspect ratio is increased, as also observed by Lim et al. [9]. But, the crack locations of solder joints on FPCB does not shift from the chip-solder interface for the 1st three geometry, and start to shift to the midpoint of the solder joint for the last 2rd geometry shape with higher aspect ratio.

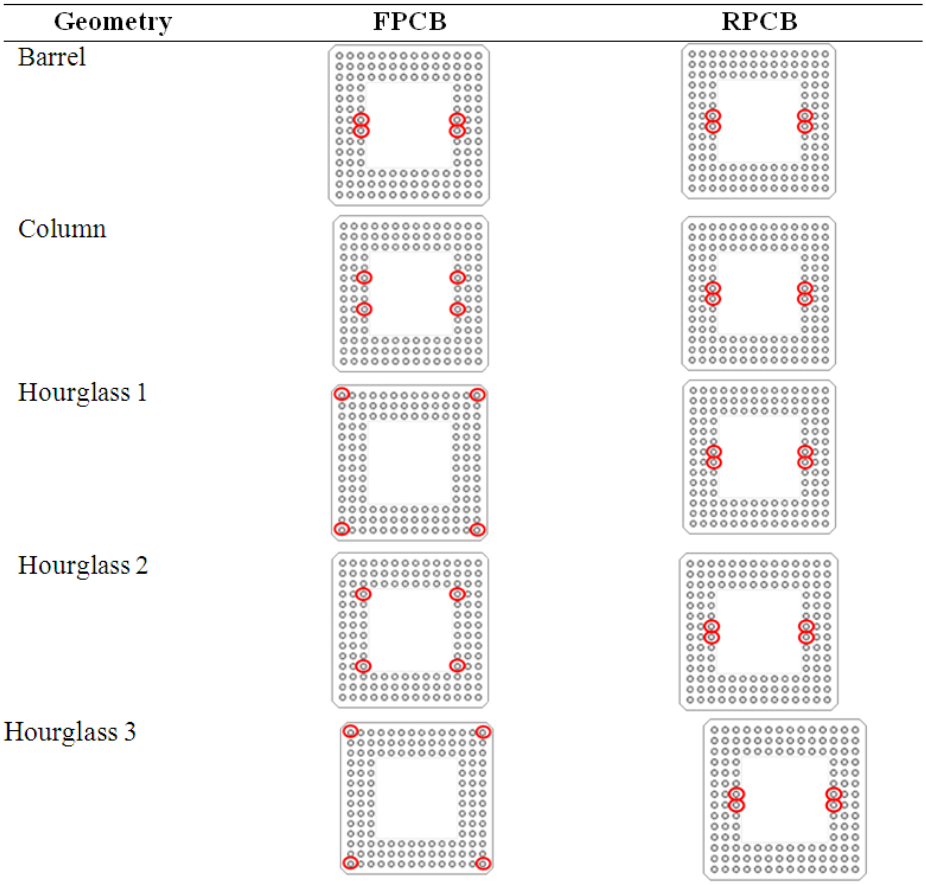

Fig. 10. Locations of Critically Affected Solder Joints on FPCB and RPCB.

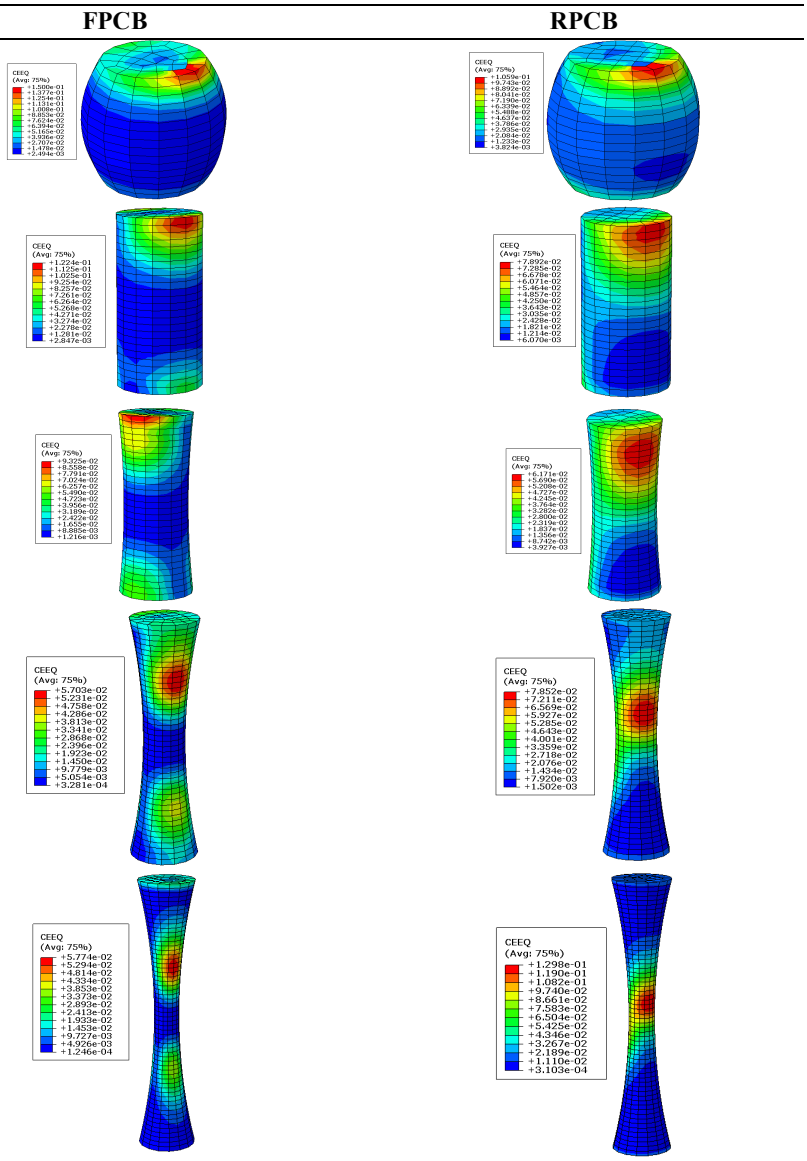

Fig. 11. The Creep Strain Profiles for Different Geometries for FPCB and RPCB.

3.5. Accumulated strain energy density (CENER)

Figure 12 shows that the accumulated volume-weighted average creep energy density of the barrel-shaped solder joint for the FPCB is higher than that of the RPCB. This observation seems a little different from the general perspective, that the increase in flexibility will improve the solder joint reliability. Some reasoning

is made based on the displacement distribution as shown in Fig. 13; for fleXBGA^{TM} package with the FPCB, the displacement distribution is non-uniform with larger magnitudes, Fig. 13(a), whereas the RPCB shows uniform displacement distribution with smaller magnitude, Fig. 13(b). Larger magnitude of PCB causes the larger warpage effect and induces the larger mismatch of coefficient of thermal expansion between the die and substrate. Thus, larger stress concentration to act on the nearest solder balls under the die, causing the creep energy density of FPCB to be larger than that of the RPCB. Besides, non-uniform displacement distribution also causes the failure locations to change, as already seen in Fig. 10. For most experiments on fleXBGA^{TM}, it was found [24] that the row of joints just outside or just underneath the die edge failed first; this substantiates the present simulation results. Similar experimental results for PBGAs were also observed by Ladani and Dasgupta [29].

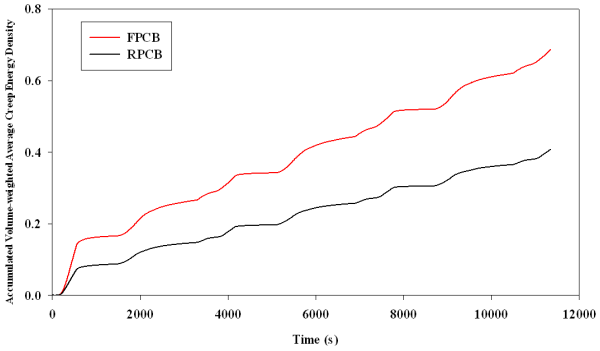

Fig. 12. Accumulated Volume-weighted Average Creep Energy Density of Barrel-shaped Solder Joint vs. Time.

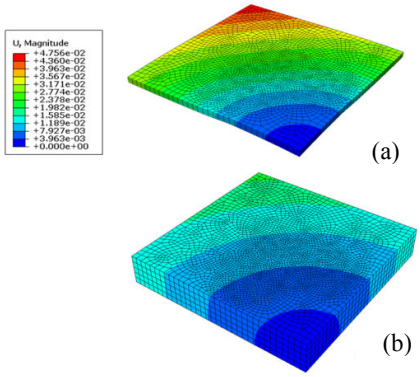

Fig. 13. The Displacement Distribution of: (a) FPCB and (b) RPCB.

3.6. Optimum solder joint geometry

For the barrel shape, crack occurs first at the corners of interfaces between solder joint and silicon die, and solders bump and substrate due to the high thermal stress concentration. However, the hourglass-shaped solder joint has much lower stress at the solder joint corners for both FPCB and RPCB; their smaller contact angle reduces the order of the singularity thereby reducing the stress and strain field near

contact edges. Moreover, the hourglass shape contributes to protecting the weak interfaces between the solder joint and the substrate, by allowing the CEEQ to move towards the middle. It was established by tensile and shear tests that that hourglass-shaped solder joint had high adhesion stress than barrel-shaped solder joint, and failed at or close to midpoint while barrel-shape failed at the interface [7].

It should be noted that, for a given solder joint volume, the advantage of protecting the weak interface by increasing the aspect ratio is countered by the threat of midpoint failure. Moreover, increasing the solder joint height without affecting the solder joint pitch is restricted by I/O density and cost. This situation calls for optimum solder joint geometry in terms of aspect ratio, strain distribution pattern and cost.

Accordingly, a comparison is made, of the maximum CEEQ of different geometries on FPCB and RPCB, as shown in Fig. 14. It is observed that for FPCB, the three hourglass shapes exhibit lower values of maximum CEEQ compared to the other two shapes; for RPCB, column, hourglass 1 and hourglass 2 are acceptable. Similar conclusion can be drawn from the comparison of accumulated strain energy density per cycle of the critical element (ΔW_{max}) as well, as illustrated in Fig. 15.

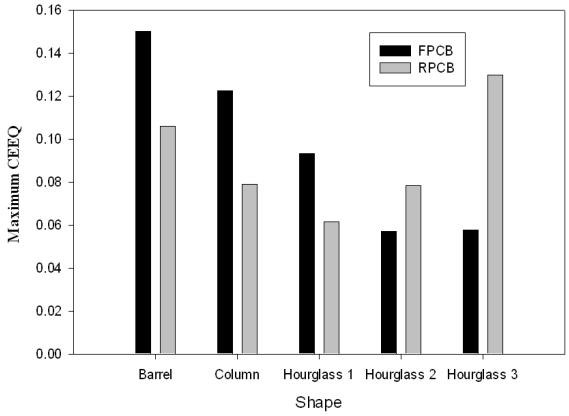

Fig. 14. Maximum CEEQ vs. Solder Joint Geometry for FPCB and RPCB.

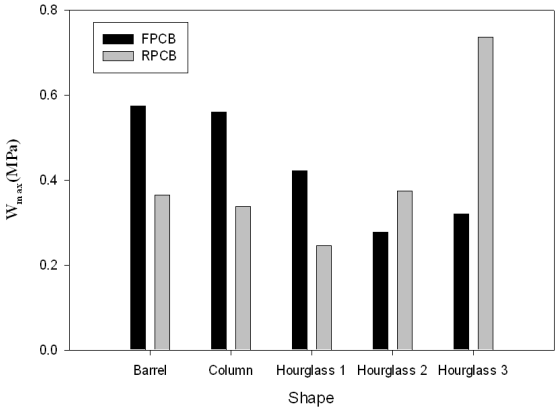

Fig. 15. ΔW_{max} (MPa) vs. Solder Joint Geometry for FPCB and RPCB.

4. Conclusions

In the present study three-dimensional (3D) finite element simulation on 132-PIN fleXBGATM package is performed to predict the effect of solder joint geometry on the reliability of BGA solder joints on flexible and rigid PCBs. The commercial FEA tool ABAQUS Version 6.9 is used for the simulations of various shapes of solder joints such as barrel, column and hourglass. The model is well validated with the published experimental data. From the global and local modeling and simulations, it is observed that the solder joint geometry significantly influences the reliability of BGA solder joints, and for a given PCB, the choice of solder joint geometry depends on its rigidity. It is also found that as the geometry changes; the locations of critically affected joints do not change on RPCB, but change on FPCB. For future work, experiments may be performed to confirm the present simulation results on FPCB. Study on the effects of solder materials (both leaded and lead-free) on the reliability of different types of geometries will also be interesting.

Acknowledgements

The authors would like to thank Universiti Sains Malaysia for the financial support for this research work.

References

1. Hannach, T.; Worrack, H.; Muller, W.H.; and Hauck, T. (2009). Creep in microelectronic solder joints: finite element simulations versus semi-analytical methods. *Archive of Applied Mechanics*, 79(6), 605-617.
2. Qian, Z.F.; and Liu, S. (1998). On the life prediction and accelerated testing of solder joints. *International Journal of Microcircuits and Electronic Packaging*, 22(4), 288-304.
3. Peng, C.T.; Chiang, K.N.; Ku, T.; and Chang, K. (2004). Design, fabrication and comparison of lead-free/eutectic solder joint reliability of flip chip package. *Proceedings of the 5th International Conference in Thermal and Mechanical Simulation and Experiments in Microelectronics and Microsystems.*
4. Arruda, L.; Bonadiman R.; Costa, J.; and Reinikainen, T. (2009). Cracking phenomena on flexible-rigid interfaces in PCBs under thermo cycling loading. *Circuit World*, 35(2), 18-22.
5. Liu, X.S.; and Lu, G.Q. (2003). Effects of solder joint shape and height on thermal fatigue lifetime. *IEEE Transactions on Components and Packaging Technologies*, 26(2), 455-465.
6. Chiang, K.N.; Lin, Y.T.; and Cheng, H.C. (2000). On enhancing eutectic solder joint reliability using a second-reflow-process approach. *IEEE Transactions on Advanced Packaging*, 23(1), 9-14.
7. Lu, G.Q.; Liu, X.S.; Wen, S.H.; Calata, J.N.; and Bai, J.G. (2004). Strategies for improving the reliability of solder joints on power semiconductor devices. *Soldering & Surface Mount Technology*, 16(2), 27-40.
8. Frank, L.; and Oien, M.A. (1988). Double-bump surface-mount technology for very high IO interconnections. *Fourth IEEE/CHMT European International in Electronic Manufacturing Technology Symposium*.

9. Lim, S.S.; Rajoo, R.; Wong, E.H.; and Hnin, W.Y. (2006). Reliability performance of stretch solder interconnections. *31st International Conference in Electronics Manufacturing and Technology*.
10. Ridout, S.; and Bailey, C. (2007). Review of methods to predict solder joint reliability under thermo-mechanical cycling. *Fatigue & Fracture of Engineering Materials & Structures*, 30(5), 400-412.
11. Akay, H.U.; Liu Y.; and Rassaian, M. (2003). Simplification of finite element models for thermal fatigue life prediction of PBGA packages. *Journal of Electronic Packaging*, 125(3), 347-353.
12. Yang, Q.J.; Shi, X.Q.; Wang, Z.P.; and Shi, Z.F. (2003). Finite-element analysis of a PBGA assembly under isothermal/mechanical twisting loading. *Finite Elements in Analysis and Design*, 39(9), 819-833.
13. Dare, A.A.; and Petinrin, M.O. (2010). Modelling of natural convection along isothermal plates and in channels using diffusion velocity method. *Maejo International Journal of Science and Technology*, 4(01), 43-52.
14. Abdul-Baqi, A.; Schreurs, P.J.G.; and Geers, M.G.D. (2005). Fatigue damage modeling in solder interconnects using a cohesive zone approach. *International Journal of Solids and Structures*, 42(3-4), 927-942.
15. Engelmaier, W. (1991). *Solder joint reliability: Theory and applications* (*Edited by J. H. Lau*). New York.
16. Desai, C.S.; and Whitenack, R. (2001). Review of models and the disturbed state concept for thermomechanical analysis in electronic packaging. *Journal of Electronic Packaging*, 123(1), 19-33.
17. Lee, H.K.; Lee, S.M.; Soo, Y.F.; and Wong, S.J. (2006). Improving solder joint reliability of WLP by means of a compliant layer. *31st International Conference in Electronics Manufacturing and Technology*.
18. Darveaux, R.; Banerji, K.; Mawer, A.; and Doddy, G. (1995). *Reliability of plastic ball grid array assembly in ball grid array technology* (*Edited by J. H. Lau*). New York.
19. Lee, W.W.; Nguyen, L.T.; and Selvaduray, G.S. (2000). Solder joint fatigue models: review and applicability to chip scale packages. *Microelectronics Reliability*, 40(2), 231-244.
20. Darveaux, R. (2000). Effect of simulation methodology on solder joint crack growth correlation. *Proceedings of 50th Electronic Components and Technology Conference*.
21. Wu, Z.H. (2012). The modeling and prediction study of BLP device solder joint three-dimensional shape. *Applied Mechanics and Materials*, 121-126, 2338-2342.
22. Amalu, E.H.; and Ekere, N.N. (2012). High temperature reliability of lead-free solder joints in a flip chip assembly. *Journal of Materials Processing Technology*, 212(2), 471-483.
23. Wei, H.; and Wang, K. (2011). A probabilistic approach to predict thermal fatigue life for ball grid array solder joints. *Journal of Electronic Materials*, 40(11), 2314-2319.
24. Darveaux, R.; Heckman, J.; Syed, A.; and Mawer, A. (2000). Solder joint fatigue life of fine pitch BGAs - impact of design and material choices. *Microelectronics Reliability*, 40(7), 1117-1127.
25. Chen, G.; and Chen, X. (2006). Finite element analysis of fleXBGA reliability. *Soldering & Surface Mount Technology*, 18(2), 46-53.

26. Wang, T.H.; and Lai, Y.S. (2005). Submodeling analysis for path-dependent thermomechanical problems. *Journal of Electronic Packaging*, 127(2), 135-140.
27. Pan, F.; and Vatanporast, R. (2005). Reliability analysis for the design of a multi-layer flexible board. *Proceedings of the 55th Electronic Components and Technology Conference*.
28. Liu, X.S. (2001). CHAPTER II Process development for solder joints on power chips. Retrieved June 30, 2012, from http://scholar.lib.vt.edu/theses/available/etd-04082001-204805/unrestricted/Chapter-2.PDF.
29. Ladani, L.J.; and Dasgupta A. (2008). Damage initiation and propagation in voided joints: modeling and experiment. *Journal of Electronic Packaging*, 130(1), 011-018.